Turk J Elec Engin, VOL.10, NO.2 2002, © TÜBİTAK

Time-Domain Simulation of Thin Material Boundaries and Thin Panels Using Digital Filters in TLM

J. PAUL, V. PODLOZNY, D. W. P. THOMAS, C. CHRISTOPOULOS
Electromagnetics Research Group, School of Electrical and Electronic Engineering
University of Nottingham, University Park, Nottingham, NG7 2RD, UNITED KINGDOM.
e-mail: jdp@eee.nottingham.ac.uk

Abstract

In this paper, the design and implementation of digital filters for the time-domain simulation of electromagnetic wave interaction with thin material boundaries and thin panels using the Transmission-Line Modelling (TLM) method are described. The technique is applied to the description of thin ferrite layers placed on the external boundaries of the modelled space and to plastic panels placed inside the modelled space. The approach is validated using one-dimensional examples having analytic solutions. Finally, the results obtained for the Shielding Effectiveness (SE) of a practical equipment enclosure are presented to demonstrate the utility of the method in Electromagnetic Compatibility (EMC) prediction.

Key Words: *Transmission line matrix, shielding effectiveness, digital filters, thin material boundaries*

1. Introduction

Transmission-Line Modelling (TLM) is a differential time-domain method for the simulation of electromagnetic wave propagation [1]. In the simulation of systems for Electromagnetic Compatibility (EMC) prediction, it is often necessary to describe frequency-dependent external boundary conditions (e.g. ferrite tiles) and/or frequency-dependent internal boundary conditions to model thin slabs of material (e.g. equipment casings or printed circuit boards). The traditional method used to describe thin layers is mesh grading, that is to reduce the cell size in the external boundary layer and/or thin panel so as to adequately model the geometry of the small feature. The disadvantages of this method are that grading errors are introduced into the solution in the form of non-physical reflections and resonances. Also, the simulation time-step is reduced to that required for stability by the smallest cell in the problem space. This means that a simulation using grading will in all cases require more time-steps. In addition, mesh grading increases the overall number of cells required for the simulation. In many practical cases, the computational run-time and memory burden may be unacceptable.

The alternative approach developed in this paper is to use a regular mesh (i.e. the cells are cubical and all of the same size) in combination with digital filters to describe the presence of frequency-dependent external boundary conditions [2, 3] and/or frequency-dependent internal boundary conditions. Application of this technique to practical problems is more likely to yield problem spaces of computationally manageable sizes and run-times than using mesh grading. Also the solution will not be corrupted by the non-physical reflections and resonances introduced by mesh grading.

The essential details of the TLM method for free-space modelling are outlined in Section 2. In Section 3, the formulation of the approach for the description of frequency-dependent external and internal boundary conditions are developed. In Section 4, the method is validated by the time-domain simulation of some simple one-dimensional (1D) cases having analytic solutions. In Section 5, the method is used to obtain the Shielding Effectiveness (SE) of an enclosure constructed from thin plastic panels. Finally, in Section 6 the conclusions of the present work are discussed.

2. Background

In this section, the TLM algorithm for the time-domain simulation of three-dimensional (3D) free-space problems is developed from Maxwell's curl equations and the constitutive relations [4].

2.1. Maxwell's curl equations for free-space

Equation (1) expresses Maxwell's curl equations in compact form.

$$\begin{bmatrix} \nabla \times \underline{H} \\ -\nabla \times \underline{E} \end{bmatrix} = \begin{bmatrix} \underline{J}_e \\ \underline{J}_m \end{bmatrix} + \frac{\partial}{\partial t} \begin{bmatrix} \underline{D} \\ \underline{B} \end{bmatrix} \tag{1}$$

The electromagnetic quantities used in this section are defined in Table 1.

Table 1. The Electromagnetic Quantities

Quantity	*Symbol*	*Units*
Electric field	$\underline{E}$	V m^{-1}
Magnetic field	$\underline{H}$	A m^{-1}
Electric current density	$\underline{J}_e$	A m^{-2}
Magnetic voltage density	$\underline{J}_m$	V m^{-2}
Electric flux density	$\underline{D}$	C m^{-2}
Magnetic flux density	$\underline{B}$	Wb m^{-2}
Free electric current density	$\underline{J}_{ef}$	A m^{-2}
Free magnetic voltage density	$\underline{J}_{mf}$	V m^{-2}
Free-space permittivity	ε_0	F m^{-1}
Free-space permeability	μ_0	H m^{-1}

In free-space, the constitutive relations for the current and flux densities are

$$\begin{bmatrix} \underline{J}_e \\ \underline{J}_m \end{bmatrix} = \begin{bmatrix} \underline{J}_{ef} \\ \underline{J}_{mf} \end{bmatrix} \quad , \quad \begin{bmatrix} \underline{D} \\ \underline{B} \end{bmatrix} = \begin{bmatrix} \varepsilon_0 \underline{E} \\ \mu_0 \underline{H} \end{bmatrix} \tag{2}$$

Substitution of (2) into (1) yields,

$$\begin{bmatrix} \nabla \times \underline{H} \\ -\nabla \times \underline{E} \end{bmatrix} - \begin{bmatrix} \underline{J}_{ef} \\ \underline{J}_{mf} \end{bmatrix} - \frac{\partial}{\partial t} \begin{bmatrix} \varepsilon_0 \underline{E} \\ \mu_0 \underline{H} \end{bmatrix} = \underline{0} \tag{3}$$

The time-domain model represents a discrete-time solution of (3), solving for the fields $\underline{E}$ and $\underline{H}$ at each time-step.

2.2. 3D TLM for free-space

In this section, the development of the TLM algorithm for free-space modelling is outlined. For simplicity, the treatment is limited to the description of regular cells iterated at the maximum time-step. The algorithm follows from the normalization of the fields $\underline{E}$ and $\underline{H}$ so that the circuit representations of these quantities $\underline{V}$ and $\underline{i}$ both have the dimensions of volts using

$$\underline{E} = -\underline{V}/\Delta\ell \quad , \quad \underline{H} = -\underline{i}/(\Delta\ell\,\eta_0). \tag{4}$$

In (4), $\Delta\ell$ is the space step and η_0 is the intrinsic impedance of free-space. Similarly, the free current densities are normalized to the quantities $\underline{i}_f$ and $\underline{V}_f$ both having the dimensions of volts using

$$\underline{J}_{ef} = -\underline{i}_f/(\Delta\ell^2\,\eta_0) \quad , \quad \underline{J}_{mf} = -\underline{V}_f/\Delta\ell^2. \tag{5}$$

Also, the time and spatial derivative operators are normalized using

$$\frac{\partial}{\partial t} = \frac{1}{\Delta t}\frac{\partial}{\partial \bar{t}} \quad , \quad (\nabla \times \ldots) = \frac{1}{\Delta\ell}(\bar{\nabla} \times \ldots). \tag{6}$$

In (6), Δt is the time-step of the time-domain simulation and $\bar{t}$ is the normalized time. In a 3D model using regular cells, the space-step and time-step are related by

$$\Delta\ell/\Delta t = 2c \tag{7}$$

where c is the speed of light in free-space. To ensure accurate modelling up to the maximum frequency of interest, f_{max}, the space-step is chosen as $\Delta\ell = c/(10 f_{max})$. Using equations (4) through (7) in (3) leads to

$$\begin{bmatrix} \bar{\nabla} \times \underline{i} \\ -\bar{\nabla} \times \underline{V} \end{bmatrix} - \begin{bmatrix} \underline{i}_f \\ \underline{V}_f \end{bmatrix} - 2\frac{\partial}{\partial \bar{t}} \begin{bmatrix} \underline{V} \\ \underline{i} \end{bmatrix} = \underline{0}. \tag{8}$$

Figure 1 shows the layout of a 3D TLM cell: It has 12 port voltages, $(V_0, V_1, \ldots, V_{11})$ on the cell boundaries and six total field quantities (E_x, E_y, E_z, H_x, H_y and H_z) at the centre of the cell. In Ref. [5] it is shown that (8) may be expressed as

$$\begin{bmatrix} V_x \\ V_y \\ V_z \\ i_x \\ i_y \\ i_z \end{bmatrix} = \frac{1}{2} \begin{bmatrix} (\,V_0 + V_1 + V_2 + V_3\,) \\ (\,V_4 + V_5 + V_6 + V_7\,) \\ (\,V_8 + V_9 + V_{10} + V_{11}\,) \\ -(\,V_6 - V_7 - V_8 + V_9\,) \\ -(\,V_{10} - V_{11} - V_0 + V_1\,) \\ -(\,V_2 - V_3 - V_4 + V_5\,) \end{bmatrix}^i - \frac{1}{4} \begin{bmatrix} i_{fx} \\ i_{fy} \\ i_{fz} \\ V_{fx} \\ V_{fy} \\ V_{fz} \end{bmatrix} \tag{9}$$

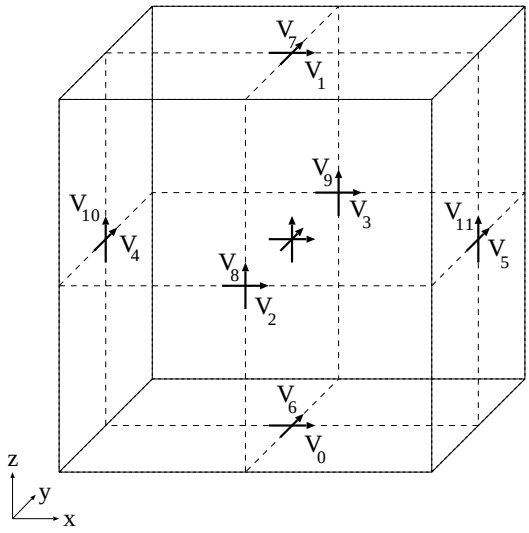

Figure 1. 3D TLM cell.

where the superscript i denotes incident wave quantities. The vector of reflected wave quantities is calculated using

$$\begin{bmatrix} V_0 \\ V_1 \\ V_2 \\ V_3 \\ V_4 \\ V_5 \\ V_6 \\ V_7 \\ V_8 \\ V_9 \\ V_{10} \\ V_{11} \end{bmatrix}^r = \begin{bmatrix} V_x - i_y - V_1^i \\ V_x + i_y - V_0^i \\ V_x + i_z - V_3^i \\ V_x - i_z - V_2^i \\ V_y - i_z - V_5^i \\ V_y + i_z - V_4^i \\ V_y + i_x - V_7^i \\ V_y - i_x - V_6^i \\ V_z - i_x - V_9^i \\ V_z + i_x - V_8^i \\ V_z + i_y - V_{11}^i \\ V_z - i_y - V_{10}^i \end{bmatrix} \tag{10}$$

where the superscript r denotes reflected wave quantities. Finally, in the connection process in (11), the reflected voltages obtained on the kth time-step at spatial index $[\bar{x}, \bar{y}, \bar{z}]$ are swapped between adjacent cells to become the incident voltages of the next time-step.

$$\underset{k+1}{\begin{bmatrix} V_1[\bar{z}-1] \\ V_0[\bar{z}+1] \\ V_3[\bar{y}-1] \\ V_2[\bar{y}+1] \\ V_5[\bar{x}-1] \\ V_4[\bar{x}+1] \\ V_7[\bar{z}-1] \\ V_6[\bar{z}+1] \\ V_9[\bar{y}-1] \\ V_8[\bar{y}+1] \\ V_{11}[\bar{x}-1] \\ V_{10}[\bar{x}+1] \end{bmatrix}^i} = \underset{k}{\begin{bmatrix} V_0 \\ V_1 \\ V_2 \\ V_3 \\ V_4 \\ V_5 \\ V_6 \\ V_7 \\ V_8 \\ V_9 \\ V_{10} \\ V_{11} \end{bmatrix}^r}, \qquad \underset{k+1}{\begin{bmatrix} V_0 \\ V_1 \\ V_2 \\ V_3 \\ V_4 \\ V_5 \\ V_6 \\ V_7 \\ V_8 \\ V_9 \\ V_{10} \\ V_{11} \end{bmatrix}^i} = \underset{k}{\begin{bmatrix} V_1[\bar{z}-1] \\ V_0[\bar{z}+1] \\ V_3[\bar{y}-1] \\ V_2[\bar{y}+1] \\ V_5[\bar{x}-1] \\ V_4[\bar{x}+1] \\ V_7[\bar{z}-1] \\ V_6[\bar{z}+1] \\ V_9[\bar{y}-1] \\ V_8[\bar{y}+1] \\ V_{11}[\bar{x}-1] \\ V_{10}[\bar{x}+1] \end{bmatrix}^r} \tag{11}$$

For cells on the external boundary of the problem space, the amplitude of the reflected voltage wave is multiplied by the voltage reflection coefficient of the boundary. For example, if there is an external boundary on the x-minimum wall of the cell illustrated in Figure 1, having a frequency independent voltage reflection coefficient of R_{x0}, the connection process would be

$$\underset{k+1}{\begin{bmatrix} V_0 \\ V_6 \end{bmatrix}}^{i} = R_{x0} \cdot \underset{k}{\begin{bmatrix} V_0 \\ V_6 \end{bmatrix}}^{r}. \tag{12}$$

In summary, the scattering process of the TLM algorithm for free-space modelling using a regular mesh iterated at the maximum time-step comprises of (9) and (10). In the next section, the modification of (11) and (12) for the description of frequency-dependent boundaries is described.

3. Formulation of Frequency-Dependent Boundary Conditions

This section describes the formulation of iteration procedures for the description of frequency-dependent external and internal boundary conditions in TLM. In both situations, the technique requires a set of data containing the analytic or measured scattering coefficients of the boundary. The frequency-domain Prony method [6] is then applied to extract approximate scattering functions in the form of sets of poles and zeroes. The bilinear $\mathcal{Z}$-transform is then applied to obtain the discrete time-domain scattering functions. These functions are implemented in the TLM simulation using state-space systems.

3.1. Frequency-dependent external boundary conditions

A boundary consisting of a slab of linear isotropic material over a perfectly conducting metal plane has a frequency-dependent reflection coefficient described by the function

$$R(s) = \frac{b_{NP} \prod_{i=0}^{NP-1} (s - s_{zi})}{\prod_{i=0}^{NP-1} (s - s_{pi})} = \frac{b_{NP}(s-s_{z0})(s-s_{z1})\cdots(s-s_{z(NP-1)})}{(s-s_{p0})(s-s_{p1})\cdots(s-s_{p(NP-1)})} \tag{13}$$

In equation (13), s is the complex frequency, NP is the number of system poles, b_{NP} is the infinite frequency gain, s_{pi} is the ith pole frequency and s_{zi} is the ith zero frequency. The Padé form is obtained by multiplying out the numerator and denominator of (13), yielding

$$R(s) \;=\; \frac{\sum_{i=0}^{NP} b_i\, s^i}{\sum_{i=0}^{NP} a_i\, s^i} \;=\; \frac{b_0 \;+\; b_1\, s \;+\cdots+\; b_{NP}\, s^{NP}}{a_0 \;+\; a_1\, s \;+\cdots+\; s^{NP}} \tag{14}$$

where the a_i and b_i coefficients are real. The next subsection outlines a method which may be used to identify these coefficients from a set of frequency-domain data.

3.1.1. Frequency-domain prony method

Given a set of NF complex frequency-domain data samples, $\{R_0, R_1, R_2, \ldots, R_{NF-1}\}$, the frequency-domain Prony method [6] yields a least-squares approximation utilizing exponential basis functions. The processing

technique identifies the coefficients a_i and b_i in (14). Rearranging (14) gives,

$$R(s)\sum_{i=0}^{NP-1} a_i\, s^i \;-\; \sum_{i=0}^{NP} b_i\, s^i \;=\; -s^{NP}\, R(s). \tag{15}$$

In the Fourier domain ($s \rightarrow j\omega$), for the sample $R_k = R(j\omega_k)$, (15) becomes,

$$R_k \sum_{i=0}^{NP-1} a_i\, (j\omega_k)^i \;-\; \sum_{i=0}^{NP} b_i\, (j\omega_k)^i \;=\; -(j\omega_k)^{NP}\, R_k. \tag{16}$$

Rewriting equation (16) for all input samples gives,

$$\underline{\underline{H}} \cdot \begin{bmatrix} a_0 \\ a_1 \\ \vdots \\ a_{NP-1} \\ b_0 \\ b_1 \\ \vdots \\ b_{NP} \end{bmatrix} \;=\; -\begin{bmatrix} (j\omega_0)^{NP}\, R_0 \\ (j\omega_1)^{NP}\, R_1 \\ \vdots \\ (j\omega_{NF-1})^{NP}\, R_{NF-1} \end{bmatrix}. \tag{17}$$

In (17), the matrix $\underline{\underline{H}} = \left[\underline{\underline{H_0}} | \underline{\underline{H_1}}\right]$, where the submatrices $\underline{\underline{H_0}}$ and $\underline{\underline{H_1}}$ are

$$\underline{\underline{H_0}} = \begin{bmatrix} R_0 & R_0(j\omega_0) & \cdots & R_0(j\omega_0)^{NP-1} \\ R_1 & R_1(j\omega_1) & \cdots & R_1(j\omega_1)^{NP-1} \\ \vdots & \vdots & & \vdots \\ R_{NF-1} & R_{NF-1}(j\omega_{NF-1}) & \cdots & R_{NF-1}(j\omega_{NF-1})^{NP-1} \end{bmatrix} \quad , \quad \underline{\underline{H_1}} = \begin{bmatrix} -1 & -j\omega_0 & \cdots & -(j\omega_0)^{NP} \\ -1 & -j\omega_1 & \cdots & -(j\omega_1)^{NP} \\ \vdots & \vdots & & \vdots \\ -1 & -j\omega_{NF-1} & \cdots & -(j\omega_{NF-1})^{NP} \end{bmatrix}. \tag{18}$$

The unknown coefficients are found by writing (17) in matrix form,

$$\underline{\underline{H}} \cdot \underline{\alpha} \;=\; -\underline{\dot{R}}. \tag{19}$$

The solution is obtained by multiplying both sides of (19) by $\underline{\underline{H}}^T$, defining the matrix $\underline{\underline{A}} = \Re\left[\underline{\underline{H}}^T \cdot \underline{\underline{H}}\right]$ and the vector $\underline{E} = \Re\left[\underline{\underline{H}}^T \cdot \underline{\dot{R}}\right]$ where $\Re[.]$ denotes the real part of $[.]$. The real parts are taken to account for the negative frequencies which are required because the calculation is performed in the Fourier domain. The vector of Padé coefficients follows from

$$\underline{\alpha} \;=\; -\underline{\underline{A}}^{-1} \cdot \underline{E} \tag{20}$$

In the application of this technique, the user must select the number of poles NP: If too many poles are selected for the approximation, matrix $\underline{\underline{A}}$ becomes ill-conditioned and if too few poles are selected, the resulting approximation is poor. Usually a few trials are needed to select the number of poles required for an accurate approximation to a particular data set.

In the solution of equation (20), the a_i and b_i coefficients of (14) have been identified. Factorizing the numerator and denominator of (14) gives the reflection coefficient in the form of equation (13). The development of the discrete-time model of (13) is detailed in the next subsection.

3.1.2. Discrete time-domain model

The discrete time-domain model of equation (13) is developed using the bilinear $\mathcal{Z}$-transform, i.e.

$$s \xrightarrow{\mathcal{Z}} \frac{2}{\Delta t}\left(\frac{1-z^{-1}}{1+z^{-1}}\right) \tag{21}$$

where z is the time shift operator. The bilinear transform of the ith zero is

$$(s - s_{zi}) \xrightarrow{\mathcal{Z}} \alpha_{zi}\left(\frac{1 - z^{-1}\beta_{zi}}{1 + z^{-1}}\right) \tag{22}$$

where the coefficients are

$$\alpha_{zi} = \frac{2 - s_{zi}\,\Delta t}{\Delta t} \qquad , \qquad \beta_{zi} = \frac{2 + s_{zi}\,\Delta t}{2 - s_{zi}\,\Delta t}. \tag{23}$$

Using (22) in (13) leads to

$$R(z) = B_0 \prod_{i=0}^{NP-1}\left[\frac{1 - z^{-1}\beta_{zi}}{1 - z^{-1}\beta_{pi}}\right] \tag{24}$$

where the coefficient

$$B_0 = b_{NP}\prod_{i=0}^{NP-1}\left(\frac{\alpha_{zi}}{\alpha_{pi}}\right). \tag{25}$$

The denominator and numerator of (24) are multiplied out to give

$$R(z) \;=\; \frac{\sum_{i=0}^{NP} B_i\, z^{-i}}{\sum_{i=0}^{NP} A_i\, z^{-i}} \;=\; \frac{B_0 + \sum_{i=1}^{NP} B_i\, z^{-i}}{1 + \sum_{i=1}^{NP} A_i\, z^{-i}} \;\xrightarrow{PFE}\; B_0 + \frac{\sum_{i=1}^{NP} B'_i\, z^{-i}}{1 + \sum_{i=1}^{NP} A_i\, z^{-i}}. \tag{26}$$

In (26), PFE represents a partial fraction expansion and the coefficients $B'_i = B_i - B_0 A_i$.

As in (12), the function $R(z)$ represents the reflection coefficient function ${}_{k+1}V^i/{}_kV^r$ of an external boundary filter, where the reflected electric field ${}_kV^r$ is the input to the filter and the incident electric field ${}_{k+1}V^i$ is the output of the filter. Suppressing the k indices and substituting these quantities into (26) gives,

$$V^i \;=\; B_0\, V^r \;+\; \frac{V^r \sum_{i=1}^{NP} B'_i\, z^{-i}}{1 + \sum_{i=1}^{NP} A_i\, z^{-i}}. \tag{27}$$

The output equation of the state-space system is

$$V^i \;=\; B_0\, V^r \;+\; \sum_{i=1}^{NP} B'_i\, X_i. \tag{28}$$

In (28), the X_i's are the state variables. Equating (27) and (28) yields the state equations,

$$\frac{V^r \sum_{i=1}^{NP} B'_i\, z^{-i}}{1 + \sum_{i=1}^{NP} A_i\, z^{-i}} \;=\; \sum_{i=1}^{NP} B'_i\, X_i \tag{29}$$

Evaluation of (29) for each variable gives,

$$X_1 = z^{-1}V^r - z^{-1}\sum_{i=1}^{NP} A_i\, X_i \quad , \quad X_2 = z^{-1}X_1 \quad , \quad X_3 = z^{-1}X_2 \quad , \ldots , \quad X_{NP} = z^{-1}X_{NP-1} \tag{30}$$

Collecting together equations (28) and (30) and expressing in matrix form yields the final system

$$V^i = B_0\, V^r + \left[\, B'_1 \;\; B'_2 \;\; B'_3 \cdots B'_{NP} \,\right] \cdot \begin{bmatrix} X_1 \\ X_2 \\ X_3 \\ \vdots \\ X_{NP} \end{bmatrix} \quad , \quad \begin{bmatrix} X_1 \\ X_2 \\ X_3 \\ \vdots \\ X_{NP} \end{bmatrix} = z^{-1}\underline{\underline{A}}' \cdot \begin{bmatrix} X_1 \\ X_2 \\ X_3 \\ \vdots \\ X_{NP} \end{bmatrix} + z^{-1} \begin{bmatrix} 1 \\ 0 \\ 0 \\ \vdots \\ 0 \end{bmatrix} V^r \tag{31}$$

In (31), the matrix $\underline{\underline{A}}'$ is

$$\underline{\underline{A}}' = \begin{bmatrix} -A_1 & -A_2 & -A_3 & \cdots & -A_{NP-1} & -A_{NP} \\ 1 & & & & & \\ & 1 & & & & \\ & & 1 & & & \\ & & & \ddots & & \\ & & & & 1 & \end{bmatrix} \tag{32}$$

Using a compact notation, the general system described by equations (31) are

$$V^i = B_0\, V^r + \underline{B}' \cdot \underline{X} \tag{33}$$

$$\underline{X} = z^{-1}\,\underline{\underline{A}}' \cdot \underline{X} + z^{-1}\,\underline{1}'\,V^r \tag{34}$$

Figure 2 illustrates (33) and (34) as a signal-flow graph.

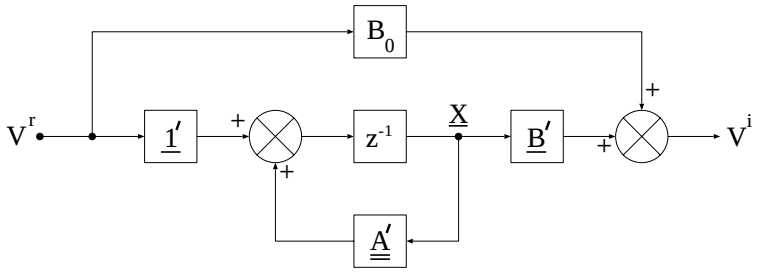

Figure 2. Signal-flow graph of an external boundary filter.

3.2. Frequency-dependent internal boundary conditions

In this section, the modification of (11) to include frequency-dependent internal boundary conditions in a TLM simulation is described. For a simple treatment, consider Figure 3 which shows two adjacent TLM cells with a thin slab of dielectric of relative permittivity ε_r, electric conductivity σ_e and thickness h placed near the boundary between the cells. The slab is positioned at a distance d_0 from the centre of the left-hand cell and d_1 from the centre of the right-hand cell.

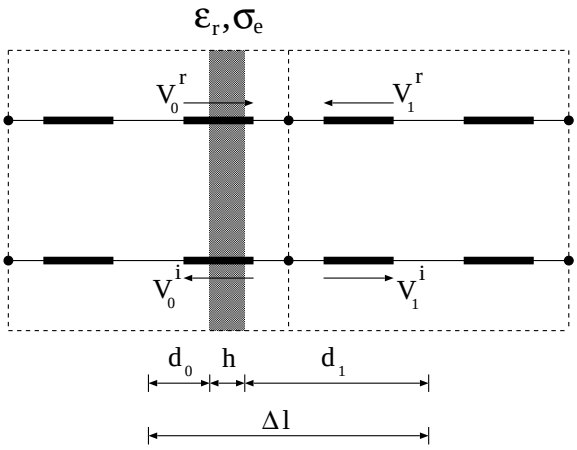

Figure 3. Modified connection process.

It can be shown from boundary matching [4] that the reflection and transmission coefficients are

$$R_{00}(s) = r\left(\frac{e^{s2\frac{h}{v}}-1}{e^{s2\left(\frac{d_0}{c}+\frac{h}{v}\right)}-r^2e^{s2\frac{d_0}{c}}}\right) \quad , \quad R_{11}(s) = r\left(\frac{e^{s2\frac{h}{v}}-1}{e^{s2\left(\frac{d_1}{c}+\frac{h}{v}\right)}-r^2e^{s2\frac{d_1}{c}}}\right) \tag{35}$$

$$T_{01}(s) = T_{10}(s) = t\left(\frac{e^{s\frac{h}{v}}}{e^{s\left(\frac{d_0+d_1}{c}+\frac{2h}{v}\right)}-r^2e^{s\frac{d_0+d_1}{c}}}\right) \tag{36}$$

where

$$r = \frac{1-\sqrt{\varepsilon_r^{\text{eff}}}}{1+\sqrt{\varepsilon_r^{\text{eff}}}} \quad , \quad v = \frac{c}{\sqrt{\varepsilon_r^{\text{eff}}}} \quad , \quad t = \frac{4\sqrt{\varepsilon_r^{\text{eff}}}}{(1+\sqrt{\varepsilon_r^{\text{eff}}})^2} \quad , \quad \varepsilon_r^{\text{eff}} = \varepsilon_r + \frac{\sigma_e}{s\,\varepsilon_0}. \tag{37}$$

The relationship between the reflected and incident voltages in the frequency-domain is

$$\begin{bmatrix} V_0 \\ V_1 \end{bmatrix}^i_{k+1} = \begin{bmatrix} R_{00} & T_{01} \\ T_{10} & R_{11} \end{bmatrix} \cdot \begin{bmatrix} V_0 \\ V_1 \end{bmatrix}^r_k \tag{38}$$

where k is the time-step index. For the simulation of the scattering coefficients of a thin slab of dielectric placed between two TLM cells, the reflection and transmission coefficients of (35) and (36) must be expressed in the $\mathcal{Z}$-domain.

The approximations of (35) and (36) are obtained using the frequency-domain Prony method described in Section 3.1.1. The approximation functions are in a Padé form, i.e.,

$$F(s) \quad = \quad \frac{\sum_{i=0}^{NP} b_i\, s^i}{\sum_{i=0}^{NP} a_i\, s^i} \quad = \quad \frac{b_0 \,+\, b_1\, s \,+\cdots+\, b_{NP}\, s^{NP}}{a_0 \,+\, a_1\, s \,+\cdots+\, s^{NP}} \tag{39}$$

where $F(s) \in \{R_{00}(s), R_{11}(s), T_{01}(s), T_{10}(s)\}$. The bilinear transform and discrete time-domain model of (39) are developed using the methods described in Section 3.1.2.

4. Validation

In this section, the methods developed in the previous section are validated using examples having analytic solutions: The external boundary conditions are tested by using the example of the normal incidence reflection coefficient of ferrite tiles. The formulation for internal boundary conditions is validated by using the example of the normal incidence reflection and transmission coefficients of a thin plastic panel.

4.1. External boundary conditions: ferrite tiles

To reduce the reflection of electromagnetic radiation from the metal walls of anechoic chambers, ferrite tiles offer excellent absorption even though they are physically thin, e.g. 6mm. For a time-domain simulation of an anechoic chamber up to a maximum frequency of 1GHz requires a space-step of $\Delta\ell = 3\,\mathrm{cm}$. Thus the ferrite tile boundaries may only be described using the approach outlined in Section 3.1.

The reflection coefficient of ferrite tiles may be identified from the material properties of the ferrite and the geometry of the tile: For a ferrite material having a constant relative permittivity ε_r, a frequency-dependent relative permeability $\mu_r(s)$ and depth d placed directly over a perfectly conducting metal surface, the reflection coefficient is [7]

$$R(s) = \frac{\eta_t(s) - \eta_0}{\eta_t(s) + \eta_0} \quad \text{where} \quad \eta_t(s) = \eta_0 \sqrt{\frac{\mu_r(s)}{\varepsilon_r}} \tanh\left(s\frac{d}{c}\sqrt{\mu_r(s)\,\varepsilon_r} \right). \tag{40}$$

Up to 1GHz, the frequency-dependence of the relative permeability of the ferrite material may be described by the function [7]

$$\mu_r(s) = 1 + \frac{\chi_{m0}\,\omega_m}{s + \omega_m}. \tag{41}$$

The frequency-dependence of the reflection coefficient function may be evaluated by the substitution of (41) into (40) and putting $s = j\omega$. Typical values for the ferrite material parameters are

$$\chi_{m0} = 337.8 \quad , \quad \omega_m = 2\pi \times 21.9 \times 10^6 \quad , \quad \varepsilon_r = 11.72 \tag{42}$$

and a typical tile depth is $d = 6.3\,\mathrm{mm}$. Using these parameters in a numerical solution of (40) gives the points labelled "Analytic" in the magnitude and phase plots shown in Figure 4.

Application of the frequency-domain Prony method described in Section 3.1.1 yields a close approximation to analysis using a two-pole model, i.e. $NP = 2$ where the coefficients required in equation (14) are

$$b_0 = -1.0976302 \times 10^{18}\,, \quad b_1 = -1.53404 \times 10^8\,, \quad b_2 = -0.474667\,, \quad a_0 = -b_0\,, \quad a_1 = 1.58047 \times 10^{10} \tag{43}$$

Solution of (14) using these coefficients yields the results labelled "Model" in Figure 4. Using a discrete-time filter as described in Section 3.1.2 in a TLM simulation using space-step $\Delta\ell = 3\,\mathrm{cm}$ and applying a Fast Fourier Transform (FFT) yielded the results labelled "TLM" in Figure 4. These figures show close agreement between the analytic solution, the frequency-domain model and the TLM solution.

4.2. Internal boundary conditions: plastic panel

Electronic apparatus is often enclosed in boxes manufactured from thin plastic sheets. Since such equipment must conform to certain EMC specifications, it is of interest to develop a technique whereby thin plastic

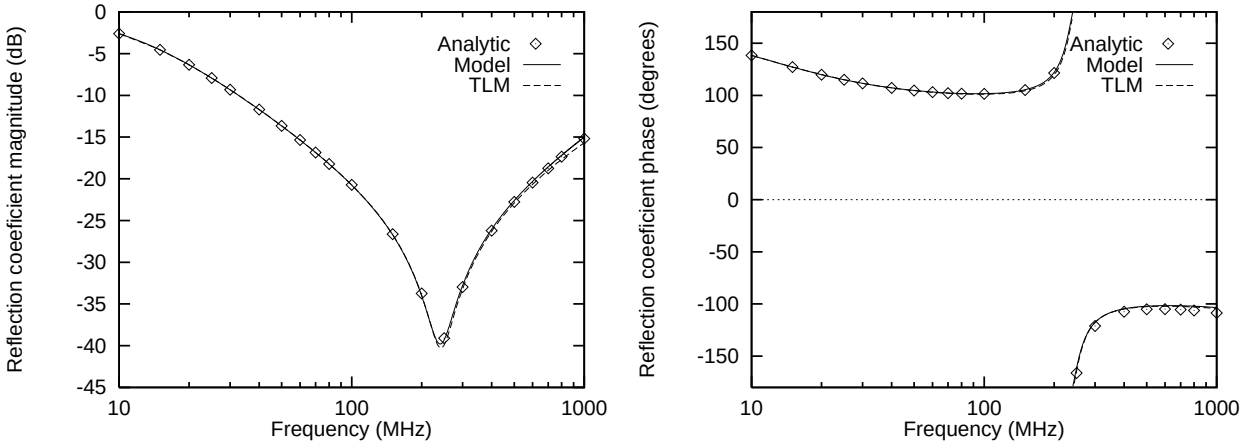

Figure 4. Normal incidence reflection coefficient magnitude and phase of ferrite tiles.

panels (i.e. thinner than the cell size) may be modelled in TLM to allow the EMC prediction of these types of enclosures. For validation purposes, consider a dielectric slab as illustrated in Figure 3, with $\varepsilon_r = 16$, $\sigma_e = 0.1\,\mathrm{S\ m^{-1}}$, $h = 2\,\mathrm{mm}$, $d_0 = 1\,\mathrm{mm}$ and $d_1 = 7\,\mathrm{mm}$. The TLM cell size $\Delta\ell = 10\,\mathrm{mm}$ so the maximum frequency of interest is $c/(10\Delta\ell) = 3\,\mathrm{GHz}$. By evaluating (35) and (36) and applying the frequency-domain Prony method, adequate approximation functions were obtained for $NP = 3$, i.e. for third-order systems. Note that although we are only interested in the frequency range up to $c/(10\Delta\ell)$, for stability the filters must satisfy the energy conservation relationship (44) up to the Nyquist frequency $c/(2\Delta\ell)$.

$$|T_{01}(\omega)||T_{10}(\omega)| + |R_{01}(\omega)||R_{10}(\omega)| \leq 1 \tag{44}$$

The coefficients used in the filters are tabulated in Table 2.

Table 2. Coefficients used in the simulation of the plastic panel

	Filter		
Coefficient	R_{00}	T_{01}/T_{10}	R_{11}
b_0	-1.28234×10^{31}	2.86873×10^{31}	-2.38819×10^{30}
b_1	-1.70192×10^{22}	2.09930×10^{20}	-3.13282×10^{21}
b_2	1.67562×10^{10}	-9.56376×10^{9}	7.52393×10^{10}
b_3	-0.179543	-0.0619411	-0.609106
a_0	3.53221×10^{32}	2.96527×10^{31}	6.60327×10^{31}
a_1	2.13669×10^{22}	2.70550×10^{21}	5.15430×10^{21}
a_2	1.99929×10^{11}	7.12978×10^{10}	1.08986×10^{11}

Figure 5 compares the magnitudes and phases of the transmission and reflection coefficients obtained from analysis, a fine mesh having $\Delta\ell = 0.1\,\mathrm{mm}$ iterated for 2^{18} time-steps and a coarse mesh having $\Delta\ell = 10\,\mathrm{mm}$ iterated for 2^{12} time-steps. The coarse mesh was augmented with the embedded filters to simulate the thin panel. Figure 5 shows close agreement in the frequency-domain between the analytic solution, the fine mesh and the coarse mesh.

In Figure 6, the time-domain response of the plastic panel for an incident Gaussian pulse was calculated using the fine and coarse meshes. The panel was positioned in the centre of the problem space and is indicated

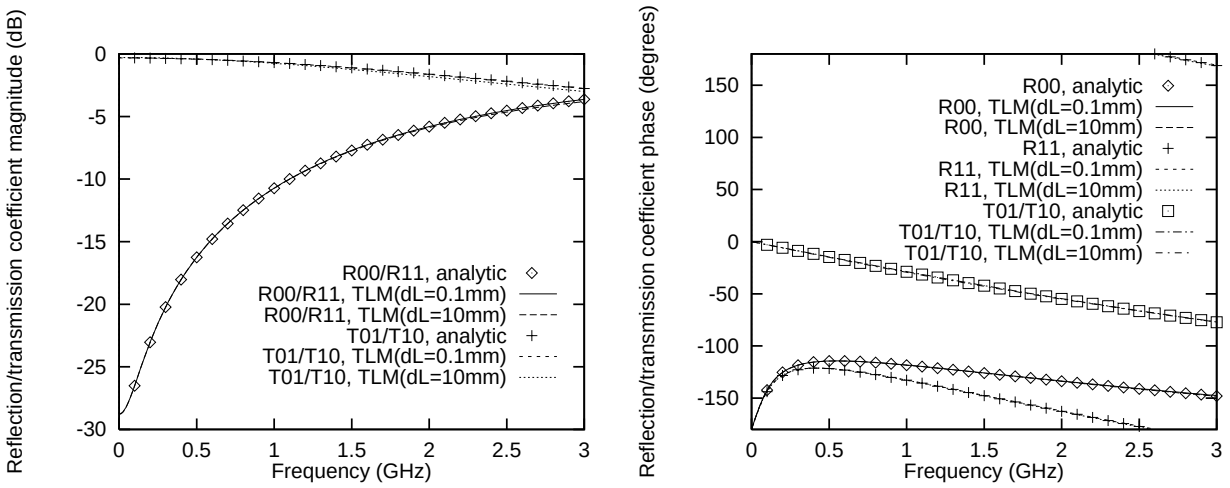

Figure 5. Reflection/transmission coefficient magnitudes and phases of the plastic panel.

by the vertical line. The fine mesh consisted of 20000 cells and was iterated for 20000 time-steps to produce the reflected and transmitted fields after 3.33ns. In contrast, the coarse mesh consisted of 200 cells with one cell containing the filters and was iterated for 200 time-steps to yield essentially the same result obtained from the fine mesh.

5. Results

In this section, the Shielding Effectiveness (SE) of an enclosure constructed from the plastic panels described in Section 4.2 is calculated. Shielding effectiveness is defined by:

$$\mathrm{SE}(f) = 20 \log_{10} \left| \frac{E_0(f)}{E_1(f)} \right| \tag{45}$$

where f is the frequency, $E_0(f)$ is the observed field at the sample point without the enclosure and $E_1(f)$ is the field observed at the sample point with the enclosure.

The modelled enclosure was cuboidal in shape having side lengths of 0.2m. The space-step was $\Delta\ell = 0.01\,\mathrm{m}$. The overall size of the computational grid was $40 \times 40 \times 40$ cells and was provided with matched conditions on the $-X$ and $+X$ external boundaries, perfect electric conductors on the $-Z$ and $+Z$ external boundaries and perfect magnetic conductors on the $-Y$ and $+Y$ external boundaries. These boundary conditions support a z-polarized plane wave propagating in the x-direction. The enclosure was placed in the centre of the modelled space and the electric field was sampled at the centre of the enclosure.

The diagram on the left-hand side of Figure 7 compares the electric field observed at the centre of the problem space with the enclosure not present with the electric field sampled at the centre of the plastic enclosure. The diagram on the right-hand side of Figure 7 shows the shielding effectiveness obtained from equation (45). This result shows that the enclosure provides about 1dB of shielding below about 0.75GHz and that the shielding is degraded to about -4dB at frequencies near 1.25GHz and 2.5GHz. The enclosure provides about 8dB of shielding at frequencies near 1.5GHz and 1.8GHz.

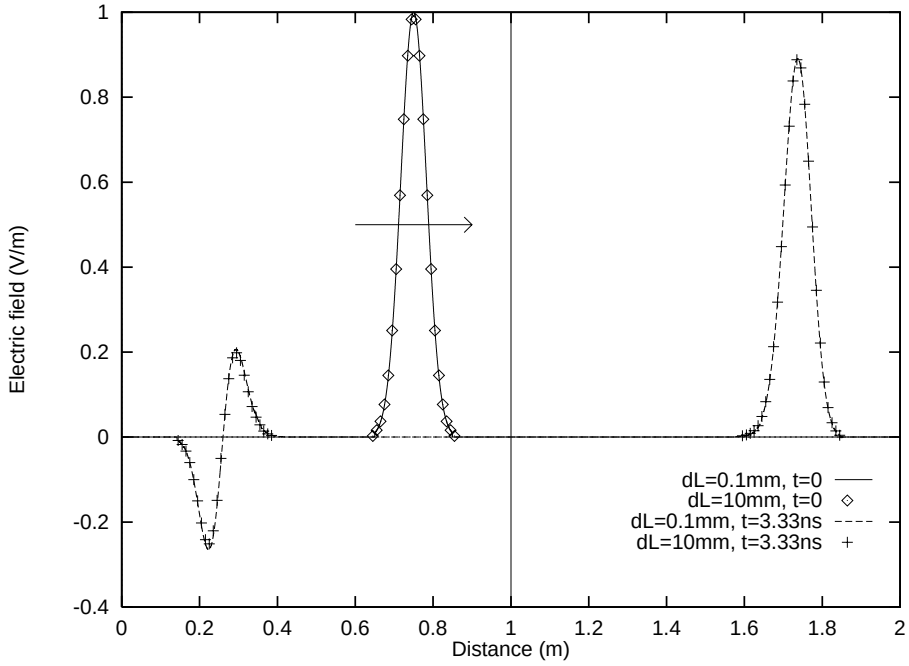

Figure 6. Time-domain response of the plastic panel.

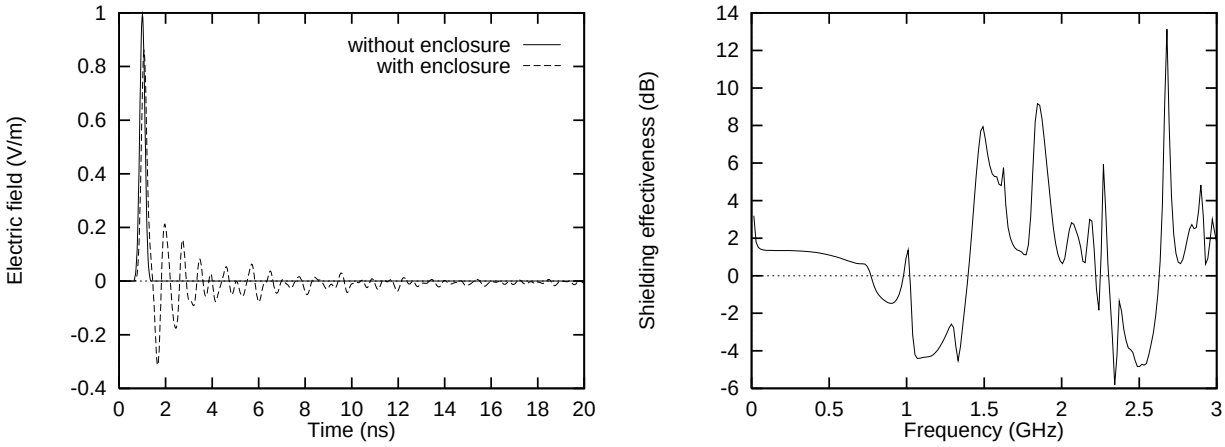

Figure 7. Electric field sampled at the centre of the enclosure and the shielding effectiveness.

6. Conclusion

This paper has described the use of digital filters for the simulation of thin boundary conditions in TLM. The use of digital filters was shown to dramatically reduce the memory burden required for the time-domain simulation of problems involving thin panels and external boundaries consisting of a thin layer of material over a perfect conductor. In addition, this approach does not suffer from corruption of the solution due to the nonphysical reflections induced on the boundaries between regions containing different size cells required with mesh-grading. Typical reductions of memory requirement by a factor of 100 in the number of spatial and temporal points required in one-dimensional simulations were achieved: In three-dimensional problems,

this yields a reduction in the number of spatial points by a factor of 10^6 and a reduction by a factor of 100 in the number of temporal points required. The digital filters were developed from frequency-domain scattering data using the frequency-domain Prony method to construct appropriate finite order scattering functions. These functions were transformed into the discrete time-domain using the bilinear $\mathcal{Z}$-transform and to ensure efficiency of the algorithm, the discrete-time filters were implemented using discrete state-space systems. The approach was validated using one-dimensional examples of external and internal boundary conditions having analytic solutions. In the final part of the paper, the method was used to find the shielding effectiveness of an equipment enclosure constructed from plastic sheets.

In further work, we intend to extend this method to the description of perforated metal plates, wire meshes, carbon-fibre composite materials and printed circuit boards.

References

[1] C. Christopoulos, *The Transmission-Line Modeling Method: TLM*. IEEE Press, Piscataway, NJ, 1995.

[2] J. F. Dawson, Representing Ferrite Absorbing Tiles as Frequency Dependent Boundaries in TLM. *Electronics Letters*, 29(9):791–792, April 1993.

[3] J. F. Dawson, J. Ahmadi and A. C. Marvin, Modelling the Damping of Screened Room Resonances by Ferrite Tiles using Frequency Dependent Boundaries in TLM. In *2nd International Conference on Computational Electromagnetics, Nottingham, UK*, pages 271–274, April 1994.

[4] J. A. Kong, *Electromagnetic Wave Theory*. Wiley, New York, 1986.

[5] J. Paul, C. Christopoulos and D. W. P. Thomas, Generalized Material Models in TLM—Part 1: Materials with Frequency-Dependent Properties. *IEEE Transactions on Antennas and Propagation*, 47(10):1528–1534, October 1999.

[6] J. N. Brittingham, E. K. Miller and J. L. Willows, Pole Extraction from Real-Frequency Information. *Proceedings of the IEEE*, 68(2):263–273, February 1980.

[7] Y. Naito and K. Suetake, Application of Ferrite to Electromagnetic Wave Absorber and its Characteristics. *IEEE Transactions on Microwave Theory and Techniques*, 19(1):65–72, January 1971.